applied sciences

MDPI

Article

Defect-Tolerant Interfacial Compatibilization of Heterogeneous Recycled Polypropylene via Binary iPP-*g*-MA/aPP-*g*-MA Masterbatches

Ruohan Liu [1], Haidi Cai [2], Zhonghua Tang [2] and Liang Tong [1,*]

[1] Jiangxi Provincial Key Laboratory of Functional Crystalline Materials Chemistry, College of Chemistry and Chemical Engineering, Jiangxi University of Science and Technology, Ganzhou 341000, China
[2] Jiangxi Yameda Technology Co., Ltd., Ganzhou 341000, China
* Correspondence: tongliang6363@jxust.edu.cn; Tel.: +8619979702070

Featured Application

The binary iPP-*g*-MA/aPP-*g*-MA masterbatch developed in this study offers a scalable compatibilization solution for mechanical recyclers processing heterogeneous post-consumer polypropylene from food-service containers. At a 2 wt% loading, the equid-weight formulation restores elongation at break to 200% and impact strength to 8.98 kJ m^{-2}, enabling the upcycled material to meet the mechanical requirements of injection-moulded semi-structural components such as storage crates, automotive interior panels, and household appliance housings.

Abstract

Single-use polypropylene (PP) food containers represent a rapidly growing waste stream characterized by compositional heterogeneity and microstructural defects. Conventional reactive compatibilization using isotactic maleic anhydride-grafted PP (iPP-*g*-MA) provides rigid crystalline anchoring but lacks the interfacial flexibility to accommodate complex micro-defects. Herein, we propose a defect-tolerant compatibilization strategy by developing a binary iPP-*g*-MA/aPP-*g*-MA masterbatch for real post-consumer rPP derived from food-service containers. The amorphous aPP-*g*-MA component is proposed to provide a compliant interfacial environment that accommodates stress concentrations associated with microscale defects, whereas the iPP-*g*-MA component contributes crystalline anchoring with the recycled PP matrix. This soft/hard interfacial architecture is supported by grafting-degree analysis, GPC, XRD, DSC crystallization behavior, and SEM fracture morphology. The 1:1 mass-ratio binary formulation shows a marked improvement in elongation at break to 200%, representing a 203% increase relative to the single-component iMA system. The notched Charpy impact strength is enhanced to 8.98 kJ m^{-2}, while tensile strength is retained at 20.9 MPa within the typical strength–ductility trade-off of polymer toughening. TGA shows no premature degradation within the melt-processing window, indicating adequate thermal stability for melt reprocessing. This study provides a compositionally tunable, data-supported route for high-value upcycling of heterogeneous post-consumer polyolefins. From an application viewpoint, the improved ductility-impact balance makes the material relevant to injection-moulded semi-structural products such as storage crates, appliance housings, and automotive interior panels.

Keywords: polypropylene; reactive compatibilization; defect tolerance; binary masterbatch; impact toughness; mechanical recycling

Check for updates

Academic Editor: Nikolaos Koukouzas

Received: 19 April 2026
Revised: 13 May 2026
Accepted: 18 May 2026
Published: 25 May 2026

Copyright: © 2026 by the authors. Licensee MDPI, Basel, Switzerland. This article is an open access article distributed under the terms and conditions of the Creative Commons Attribution (CC BY) license.

1. Introduction

Single-use polypropylene (PP) food-service containers represent one of the most rapidly growing streams of post-consumer plastic waste in urban municipal solid waste systems. PP accounts for approximately 19% of global plastics production, and a disproportionate fraction of this output is directed toward short service-life packaging [1,2]. Despite the material homogeneity that nominally favours PP recyclability, recycled PP (rPP) derived from food-service containers presents a particularly challenging feedstock compared with other PP waste streams [3]. This difficulty primarily arises from accelerated thermo-oxidative degradation during service, including microwave or hot-fill thermal exposure, and the compositional heterogeneity associated with commingled collection [4–6]. Collectively, these factors manifest in the recycled product as complex microstructural defects, elevated polar group content, shortened molecular chains, and a pronounced loss of impact toughness relative to virgin isotactic PP (iPP). The transition from nominally homogeneous virgin PP to heterogeneous rPP is therefore associated with thermal history, oxidative chain scission, residual additives, inorganic residues, and interfacial micro-defects generated during post-consumer use and collection.

Reactive compatibilization via maleic anhydride-grafted PP (iPP-*g*-MA) remains the most industrially adopted approach to restore matrix cohesion in mechanically recycled polyolefins [7]. The succinic anhydride moieties generated by peroxide-initiated melt grafting enable covalent or hydrogen-bonding interactions with oxidised chain ends and residual polar contaminants [8,9]. All commercially available PP-*g*-MA compatibilizers are based on isotactic PP backbones. While iPP-*g*-MA effectively improves the tensile stiffness of rPP compounds, the high degree of crystallinity and the rigid lamellar microstructure intrinsic to the iPP backbone, a direct consequence of the β-scission-limited grafting chemistry [10], provide limited capacity for energy dissipation under impact loading. Crucially, this structural rigidity severely restricts the ability of iPP-*g*-MA to conform to and accommodate the highly heterogeneous and defective interfaces characteristic of severely degraded rPP, leaving elongation at break and impact strength below virgin benchmarks. These limitations motivate a compatibilizer design that combines crystalline anchoring with local interfacial compliance, rather than relying solely on a rigid isotactic PP-*g*-MA backbone.

Atactic PP (aPP) possesses a statistically random methyl-group configuration that suppresses crystallization entirely, yielding a fully amorphous viscoelastic material with high chain-segment mobility and remarkable ductility [11]. This inherent structural flexibility and absence of crystalline constraints provide a latent reservoir for energy dissipation. Zhou et al. demonstrated that the incorporation of aPP into iPP matrices can simultaneously enhance tensile strength and impact toughness under controlled loading and processing conditions [12]. Despite this mechanistic rationale, aPP-*g*-MA has not been evaluated as a compatibilizer component for highly heterogeneous rPP systems. The potential synergy of combining iPP-*g*-MA with aPP-*g*-MA to construct a defect-tolerant binary compatibilizer has not been sufficiently explored.

The present study addresses this gap by developing a dual-component compatibilizer strategy designed to form a proposed compliant/crystalline interfacial structure rather than a directly measured modulus gradient. Specifically, the amorphous aPP-*g*-MA segments are expected to enhance local interfacial compliance to accommodate microscale structural defects and polar degradation products, promoting localized energy dissipation. Concurrently, the iPP-*g*-MA component co-crystallizes with the rPP matrix to ensure robust mechanical anchoring. To examine this structure–property relationship, the interfacial chemical structure, crystalline morphology, and thermodynamic phase transitions were systematically investigated using Fourier-transform infrared spectroscopy (FTIR), X-ray diffraction (XRD), and differential scanning calorimetry (DSC). The macroscopic mechanical

response and microscopic fracture mechanisms were elucidated through mechanical testing and scanning electron microscopy (SEM). The results show that the equal-weight binary formulation improves elongation at break and notched impact strength while retaining tensile strength, supporting the proposed defect-tolerant compatibilization mechanism. These findings establish a compositionally tunable, data supported route for the high value upcycling of heterogeneous post-consumer PP waste.

2. Materials and Methods

2.1. Materials

Isotactic polypropylene, designated as iPP with a weight-average molecular weight of approximately 250,000 g mol^{-1} and a melt flow index of 3.0 g/10 min at 230 °C and 2.16 kg, was supplied by BASF (China) Company Ltd., Shanghai, China. Low-molecular-weight atactic polypropylene, atactic polypropylene, designated as aPP and analysed as fully amorphous with a weight-average molecular weight of approximately 4208 g mol^{-1}, was supplied by Sigma-Aldrich, St. Louis, MO, USA. Maleic anhydride with a purity of at least 99% and benzoyl peroxide with a purity of at least 98% were obtained from Sigma-Aldrich, St. Louis, MO, USA. Antioxidant Irganox 1010, chemically identified as pentaerythritol tetrakis [3-(3,5-di-tert-butyl-4-hydroxyphenyl)propionate], was supplied by BASF (China) Company Ltd., Shanghai, China. Plate-like Talc powder with a purity of at least 98% was supplied by Haicheng Haiming Mining Co., Ltd., Haicheng, Liaoning, China, and used as received as a mineral filler. A commercial iPP-based PP-*g*-MA with a grafting degree of approximately 1.0 wt%, hereafter referred to as the Commercial benchmark, was purchased from Eastman Chemical Company, Kingsport, TN, USA, and used as received. Detailed commercial molecular-weight and MFI data were not disclosed by the supplier. All reagents were used as received without further purification unless otherwise stated.

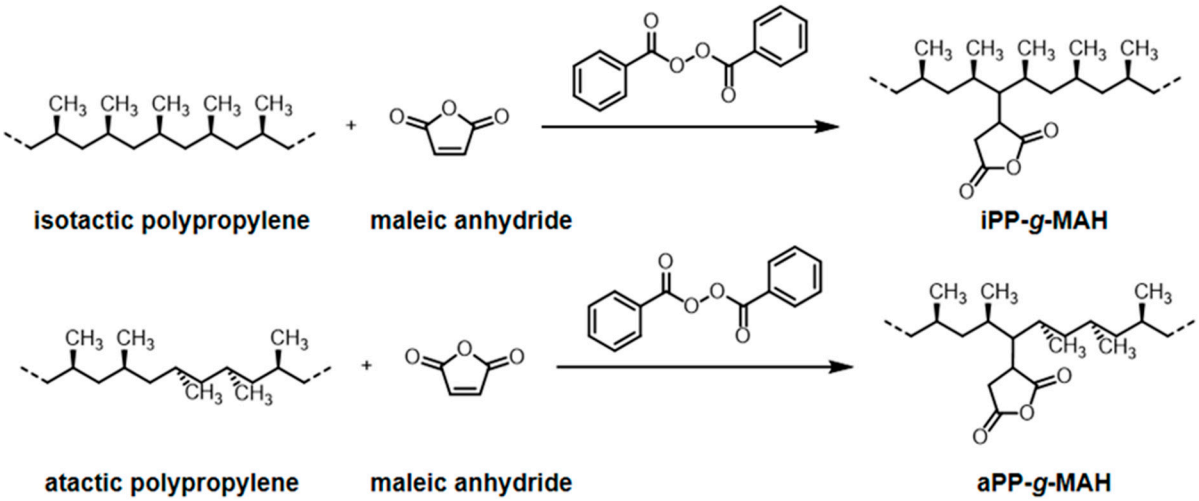
Post-consumer recycled polypropylene, referred to as rPP, was sourced from mechanically recycled single-use disposable meal containers collected through a municipal solid waste recovery programme. The feedstock was pre-sorted by infrared-based automated sorting to confirm its identity as polypropylene, washed with warm water at 60 °C for 15 min to remove food residues, rinsed with deionised water, and dried at 80 °C under vacuum for 12 h prior to processing. No additional purification or compatibilization was applied to the rPP feedstock before compounding. The selection criterion for this feedstock was its practical representativeness of mechanically recycled PP food-container waste: polymer identity was confirmed by infrared sorting, visible non-PP contaminants were removed during sorting, and the material was intentionally used without further purification to preserve the heterogeneity of an industrial recycling stream.

2.2. Synthesis of iPP-g-MA and aPP-g-MA

iPP-*g*-MA and aPP-*g*-MA were independently synthesised by reactive melt grafting in a co-rotating twin-screw extruder (HAAKE MiniLab III, Thermo Fisher Scientific, Karlsruhe, Germany) featuring a length-to-diameter ratio of 40 and a screw diameter of 20 mm. The reactive melt grafting process is schematically illustrated in Scheme 1, Prior to extrusion, the respective PP pellets were dry-blended with MAH at a concentration of 2 wt% and BPO at 0.3 wt% relative to the PP matrix in a high-speed mixer at room temperature for 10 min to achieve uniform surface coating.

The coated pellets were fed into the extruder and processed at a barrel temperature profile of 180 °C feed to die, screw speed of 80 rpm, and a throughput of approximately 1.0 kg h^{-1}. Nitrogen purging was maintained throughout to suppress oxidative side reactions. The extrudate was pelletised and subsequently purified to remove unreacted MAH homopolymer and residual monomer. Purification was performed by Soxhlet extraction

with acetone for 12 h, followed by filtration, washing three times with fresh acetone, and drying at 60 °C under vacuum for 24 h. The grafting degree (GD) of the purified products was determined by ^{1}H NMR spectroscopy and corroborated by alkaline back-titration using a previously reported titration procedure. The final products, designated iPP-*g*-MA and aPP-*g*-MA, were stored under dry conditions at room temperature prior to use.



Scheme 1. Schematic illustration of the reactive melt grafting of maleic anhydride onto isotactic and atactic polypropylene initiated by BPO.

Mechanistically, BPO acts as a radical initiator during melt grafting. Upon thermal decomposition, BPO generates benzoyloxy radicals that abstract hydrogen atoms from tertiary C-H sites on the PP backbone, producing PP macroradicals. These macroradicals subsequently add to the electron-deficient double bond of maleic anhydride, forming grafted succinic anhydride-derived groups on the PP chain. The effective grafting outcome was evaluated from the grafting degree determined by alkaline back-titration and corroborated by ^{1}H NMR, while GPC was used to assess molecular-weight changes associated with peroxide-induced chain scission.

2.3. Preparation of Compatibilizer Masterbatches and rPP Compounds

Three binary compatibilizer formulations were prepared by melt-blending iPP-*g*-MA and aPP-*g*-MA at weight ratios of 100/0, 50/50, and 0/100, designated iMA, biMA, and aMA, respectively. Blending was carried out in the twin-screw extruder at 185 °C and 80 rpm. The resulting masterbatch pellets were dried at 80 °C for 8 h before compounding.

rPP compounds were prepared by melt-compounding rPP (93 wt%) with 2 wt% of each compatibilizer masterbatch (iMA, biMA, aMA, or the Commercial benchmark) and 5 wt% talc in a single co-extrusion step in the twin-screw extruder at 185 °C and 80 rpm. All three components were pre-dried at 80 °C for 8 h and tumble-blended for 10 min before feeding. The extrudate was water-bath quenched, pelletised, and dried at 80 °C for 12 h. The compatibilizer loading was fixed at 2 wt% to reflect a low-addition, industrially relevant formulation and to avoid excessive plasticization or cost increase while maintaining measurable interfacial effects.

2.4. Sample Preparation

Standard test specimens were fabricated by injection moulding using an all-electric injection moulding machine model Arburg Allrounder 270S from Arburg, Lossburg, Germany. Processing conditions were as follows: melt temperature 200 °C, mould temperature 40 °C, injection pressure 80 MPa, holding pressure 60 MPa for 10 s, and cooling time 20 s.

Dumbbell-shaped tensile specimens conforming to ISO 527-2 type 1B and rectangular bars for notched Charpy impact testing measuring 80 by 10 by 4 mm according to ISO 179-1 were moulded. Specimens were conditioned at 23 °C and 50% relative humidity for 48 h prior to mechanical testing. For SEM analysis, tensile specimens were fractured under liquid nitrogen following tensile testing and stored in a desiccator prior to sputter-coating.

2.5. Characterization

2.5.1. Fourier-Transform Infrared Spectroscopy

FTIR spectra were collected using an attenuated total reflectance accessory on a Thermo Fisher Scientific Nicolet iN10 spectrometer from Thermo Fisher Scientific, Madison, WI, USA. Spectra were recorded over the range 4000–400 cm^{-1} at a resolution of 4 cm^{-1} with 32 co-added scans per spectrum. The carbonyl-related band in the 1710–1725 cm^{-1} region was analyzed relative to the PP C–H bending reference band at approximately 1456 cm^{-1}, rather than the non-standard 2722 cm^{-1} band. All spectra were baseline-corrected and normalised prior to comparison.

2.5.2. X-Ray Diffraction

X-ray diffraction patterns were obtained on a Bruker D8 Advance diffractometer from Bruker, Karlsruhe, Germany, equipped with a Cu Kα radiation source having a wavelength of 0.15406 nm operating at 40 kV and 40 mA. Diffraction patterns were recorded over a 2θ range of 5–70° at a scan rate of 2° min^{-1} with a step size of 0.02°. Compression-moulded films with a thickness of approximately 0.5 mm were used as specimens. The degree of crystallinity (X_c) was estimated from peak deconvolution by the ratio of the integrated crystalline diffraction area to the total scattering area.

2.5.3. Differential Scanning Calorimetry

DSC measurements were performed on a TA Instruments DSC 250 from TA Instruments, New Castle, DE, USA, under a nitrogen atmosphere at a flow rate of 50 mL min^{-1}. Specimens of 5–8 mg were encapsulated in aluminium pans and subjected to the following thermal programme: (i) heating from 25 °C to 200 °C at 10 °C min^{-1}; (ii) isothermal hold at 200 °C for 5 min to erase thermal history; (iii) cooling to −20 °C at 10 °C min^{-1}; (iv) second heating to 200 °C at 10 °C min^{-1}. Melting temperature (T_m), crystallisation temperature (T_c), and enthalpy of fusion (ΔH_m) were extracted from the second heating and first cooling cycles, respectively. The degree of crystallinity was calculated as $X_c = \Delta H_m / (\Delta H_{0m} \times wPP)$, where ΔH_{0m} = 209 J g^{-1} is the theoretical enthalpy of fusion of 100% crystalline iPP and wPP is the weight fraction of PP in the compound.

2.5.4. Thermogravimetric Analysis

TGA was conducted on a Mettler Toledo TGA 2 analyser from Mettler Toledo, Selb, Germany. Specimens of approximately 8 mg were heated from 30 °C to 600 °C at a rate of 10 °C min^{-1} under a nitrogen flow of 20 mL min^{-1}. The onset decomposition temperature, defined at 2 wt% mass loss and denoted as Tonset, along with the peak decomposition temperature, derived from the DTG maximum and denoted as T_{peak}, and residual char at 600 °C were recorded. All measurements were performed in triplicate.

2.5.5. Mechanical Testing

Uniaxial tensile tests were performed on an Instron 5966 universal testing machine from Instron, Norwood, MA, USA, equipped with a 10 kN load cell, at a crosshead speed of 50 mm min^{-1} in accordance with ISO 527-2. Tensile strength (TS), elongation at break (EB), and Young's modulus were determined from the resulting stress–strain curves. A minimum of five specimens per formulation were tested and results are reported as mean ± standard

deviation. Notched Charpy impact strength (IS) was measured on a Zwick/Roell HIT25P pendulum impact tester from Zwick/Roell, Ulm, Germany, according to ISO 179-1 under edgewise conditions with a type A notch at 23 °C. A minimum of ten specimens were tested per formulation.

2.5.6. Scanning Electron Microscopy

Fracture surfaces of tensile specimens were examined using a Carl Zeiss ΣIGMA field-emission SEM from Carl Zeiss AG, Oberkochen, Germany, at an accelerating voltage of 15 kV with a secondary electron detector. Prior to imaging, specimens were sputter-coated with a 10 nm gold–palladium layer using a Quorum Q150R sputter coater from Quorum Technologies, Laughton, UK, to minimise charge accumulation. Images were acquired at magnifications of 300×, 2000×, and 10,000× to capture fracture morphology at multiple length scales.

2.5.7. Gel Permeation Chromatography

Gel permeation chromatography (GPC) was performed on the purified grafted compatibilizers to evaluate molecular-weight changes associated with peroxide-initiated melt grafting. The number-average molecular weight (Mn), weight-average molecular weight (Mw), and dispersity (Đ = Mw/Mn) were calculated from the calibrated chromatograms. The resulting data were used as an additional indicator of chain scission during grafting and to avoid overinterpreting the grafted products as structurally unchanged PP backbones.

3. Results

3.1. Chemical Structure and Interfacial Interactions

FTIR spectroscopy provides qualitative evidence consistent with successful maleic anhydride grafting and elucidates the local chemical environment of the compatibilizers. As depicted in Figure 1a, unmoulded PP backbones lack absorption in the 1700–1800 cm^{-1} region prior to modification. Following reactive extrusion, the compatibilizers iMA, aMA, and the binary blend biMA show a weak carbonyl absorption band or shoulder in the 1710–1725 cm^{-1} region, which is assigned to the C=O stretching vibration of grafted maleic anhydride-derived groups. Because this carbonyl absorption is weak at the low grafting level used in this study, the actual grafting degree was further quantified by alkaline back-titration and corroborated by ^{1}H NMR. Concurrently, the characteristic C–H stretching vibrations near 2933 and 2973 cm^{-1} remain unchanged, indicating that the main PP backbone features are retained after grafting.

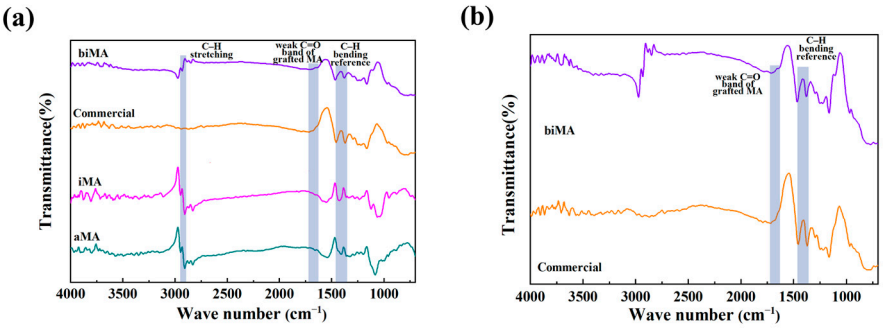


Figure 1. (**a**) FTIR spectra of iPP, aPP, iPP-*g*-MA, aPP-*g*-MA, and biMA stacked, highlighting C=O region 1650–1800 cm^{-1} and CH_2 reference region; (**b**) FTIR comparison of biMA versus Commercial PP-*g*-MA, same wavenumber range. The shaded region at 1710–1725 cm^{-1} indicates the weak C=O absorption band assigned to grafted maleic anhydride-derived groups. The shaded regions near 2930–2970 cm^{-1} and approximately 1456 cm^{-1} correspond to PP C–H stretching and the C–H bending reference band, respectively.

The grafting degrees of the three compatibilizer masterbatches, determined by alkaline back-titration and corroborated by ^{1}H NMR, are 1.89%, 1.92%, and 1.94% for iMA, biMA, and aMA, respectively (Table 1), values within the range reported for conventional reactive extrusion processes [13]. The GD values of iPP-*g*-MA and aPP-*g*-MA are now summarized in tabular form, together with the GPC-derived molecular-weight data of the synthesized compatibilizers. The marginally higher GD of aMA relative to iMA (0.05 percentage points) reflects the fully amorphous character of the aPP backbone: the absence of crystalline lamellae allows unrestricted radical access to tertiary C–H sites along the entire chain, whereas in iPP the ordered crystalline regions impose a steric barrier that effectively reduces the concentration of reactive sites accessible during the melt-phase grafting window. The GPC profiles (Figure 2) show that the grafted products retain polymeric molecular-weight distributions after peroxide-initiated grafting, although β-scission during reactive extrusion cannot be fully excluded. The near-identical GD of biMA and the arithmetic mean of the two individual components (1.915%) suggests that no significant inter-chain cross-reactivity occurs during co-processing of the two polymer types, consistent with the short radical lifetimes at 185 °C [8,9].

Table 1. Grafting degree and GPC molecular-weight data of the synthesized compatibilizers.

Sample	iPP-*g*-MA/aPP-*g*-MA Ratio	GD (wt%)	Mn (g mol^{-1})	Đ
iMA	100/0	1.89	66,600	1.76
biMA	50/50	1.92	-	-
aMA	0/100	1.94	9700	2.77

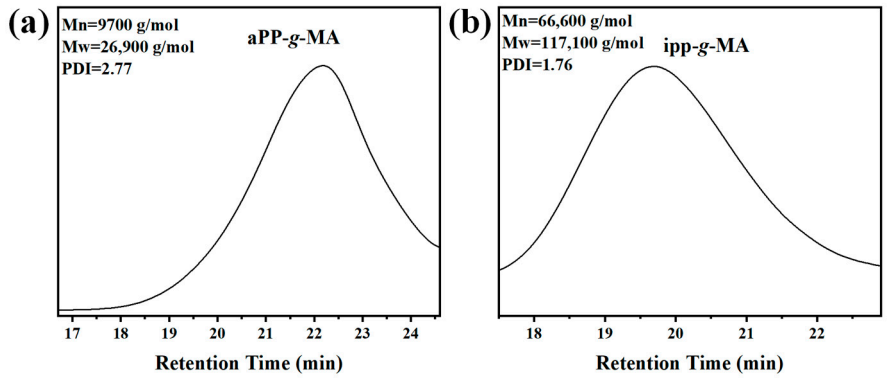


Figure 2. GPC molecular-weight distribution profiles of (**a**) aPP-*g*-MA and (**b**) iPP-*g*-MA compatibilizers after peroxide-initiated grafting.

3.2. Crystalline Microstructure and Interphase Morphology

The crystallographic structure and thermal phase transitions of the rPP compounds provide indirect structural information related to the proposed defect-tolerant interphase. XRD patterns (Figure 3a) confirm that all samples maintain the characteristic α-crystal reflections of isotactic PP at 2θ = 14.1°, 17.0°, 18.6°, and 21.2°. Additional reflections common to all four formulations, notably at 2θ = 9.4°, 19.3°, and 28.6°, are attributed to the basal planes of the talc mineral filler [14]. A critical structural deviation emerges at 2θ = 16.1°, corresponding to the β(300) reflection. The Commercial reference formulation exhibits negligible β-phase content. The incorporation of aPP-*g*-MA in the biMA and aMA systems induces a distinct accumulation of the metastable β-crystal polymorph [15]. The amorphous aPP segments may act as nucleation-disrupting diluents at the crystal growth front, restricting the highly ordered lateral packing of α-lamellae and creating a localised environment kinetically favourable for β-crystal formation. This β-phase accumulation occurs in the presence of talc, a well-documented α-nucleating agent, suggesting that the

amorphous aPP-*g*-MA segments influence local crystallization behavior at the interphase. Given that β-spherulites possess inherently superior plastic deformation capabilities, their enrichment at the interface may contribute to energy dissipation and crack blunting near heterogeneous defect sites of the rPP matrix.

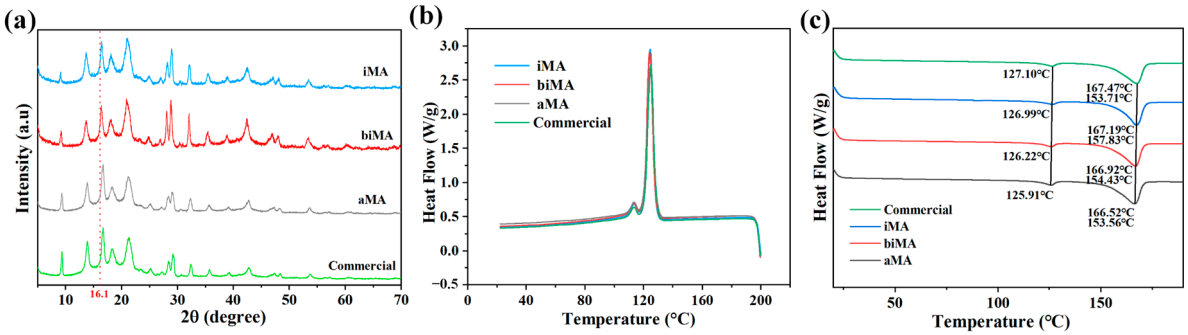


Figure 3. (**a**) Stacked XRD patterns of iMA, biMA, aMA, and Commercial indicating α-crystal peaks and the β-crystal 16.1° position; (**b**) DSC first cooling curves indicating T_c for each sample; (**c**) DSC second heating curves from 25 to 200 °C indicating T_{m1} and T_{m2} for each sample.

The DSC cooling curves (Figure 3b) characterize the melt-solidification kinetics. All formulations display a primary crystallization peak (T_c) near 125 °C. The minor suppression of crystallization efficiency in the presence of aPP-*g*-MA suggests that the amorphous compatibilizer segments may retain local mobility during the cooling window, which could facilitate wetting of defect-rich or polar interfacial regions before complete structural arrest of the matrix.

DSC heating curves (Figure 3c) provide indirect thermal evidence consistent with the proposed formation of a structurally graded interphase. The biMA, iMA, and aMA compounds exhibit a pronounced double-melting profile. The high-temperature endotherm (T_{m2}, ~167 °C) corresponds to the melting of the mature, highly ordered α-crystalline lamellae of the bulk rPP matrix. The prominent low-temperature endotherm (T_{m1}, ~126–127 °C) represents the melting of thinner, less-perfect crystallites localised at the phase boundaries. These low-perfection crystalline populations may act as more yieldable structural anchors that bridge the rigid bulk matrix and the softer amorphous interfacial component.

3.3. Thermal Stability and Processing Reliability

TGA and DTG were conducted to evaluate the thermal degradation behaviour of the compatibilized rPP compounds. As illustrated in Figure 4a,b, all four formulations exhibit a highly consistent, single-step thermal decomposition profile in the temperature range of 380–490 °C. This characteristic mass loss is primarily governed by the random chain scission of the polypropylene matrix. T_{peak} extracted from the DTG maxima remain closely clustered around 452–455 °C for all samples, indicating that the compatibilizer architecture does not introduce a new low-temperature degradation pathway.

Crucially, the incorporation of the fully amorphous aPP-*g*-MA component in the biMA and aMA systems does not induce any premature or secondary low-temperature degradation events. Here, premature degradation was defined as an additional mass-loss step or DTG shoulder below the typical PP melt-processing range. A potential concern with utilising amorphous segments is a reduction in thermal resistance. However, the curves demonstrate that the structural flexibility required for establishing the proposed defect-tolerant interphase is achieved without compromising the thermal integrity of the compounds. The absence of low-temperature mass loss within the typical processing window of PP (approximately 180–240 °C) is more practically relevant than the peak degradation temperature alone and supports the suitability of the compounds for melt re-

processing. Direct DMA or glass-transition measurements were not included in the present revision; therefore, the discussion of aPP-*g*-MA mobility is presented as an interpretation based on its amorphous structure, DSC/XRD behavior, and fracture morphology, rather than as a directly measured dynamic-mechanical property.

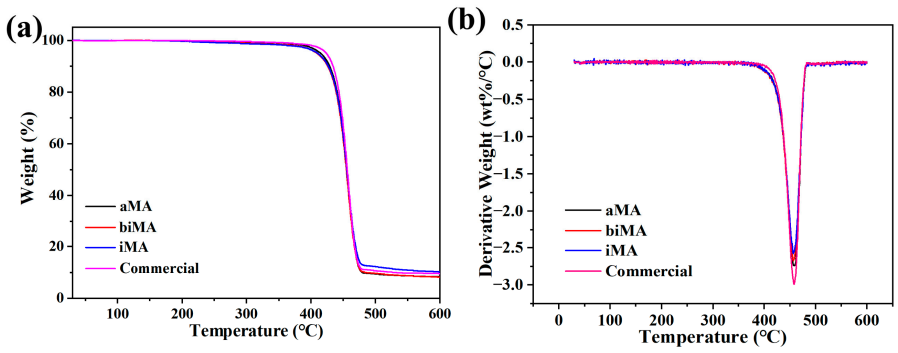


Figure 4. (**a**) TGA mass-loss curves and (**b**) DTG curves indicating T_{peak} for all rPP compounds.

The residual char content at 600 °C stabilises at approximately 8–11 wt% across all samples. This residue primarily reflects the 5 wt% talc loading together with the inorganic fillers and carbonaceous impurities inherent to the post-consumer meal container feedstock. The similar residue content alone is not sufficient to prove an identical degradation mechanism, but together with the single-step TGA/DTG profiles, it suggests that the compatibilizer architecture does not substantially alter the overall thermal degradation pathway.

3.4. Rheological Behaviour, Mechanical Properties, and Defect Tolerance

The melt flow index, uniaxial tensile, and notched Charpy impact performance of the compatibilized rPP compounds are summarised in Figure 5. These metrics are considered in sequence to establish the rheological baseline for processing, the load-bearing capacity, and the energy-dissipation response.

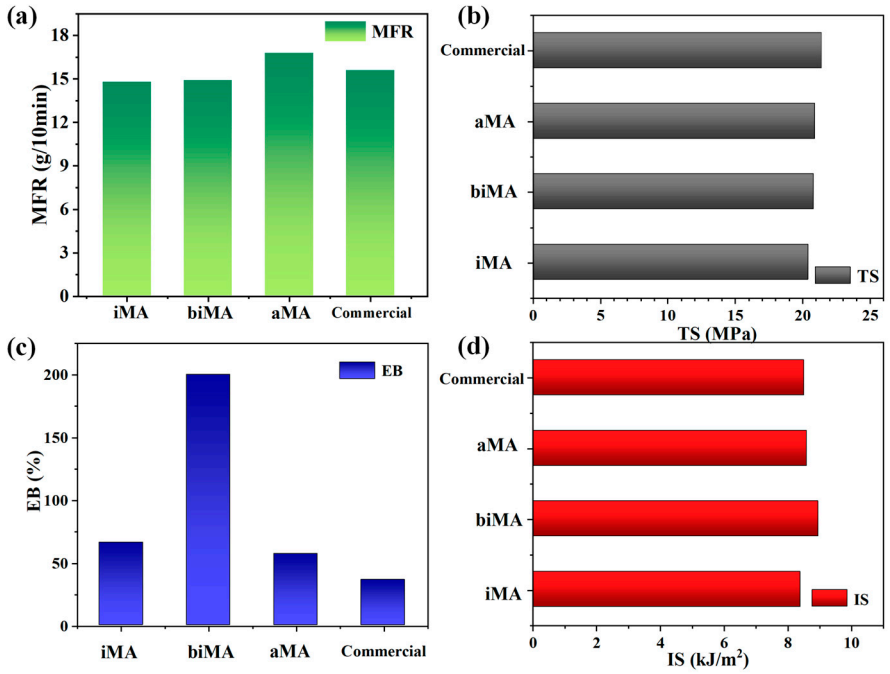


Figure 5. Rheological and mechanical performance of the rPP compounds: (**a**) melt flow index measured at 230 °C under a 2.16 kg load; (**b**) tensile strength; (**c**) elongation at break; (**d**) notched Charpy impact strength. All error bars represent the standard deviation of the mean.

The melt flow index, uniaxial tensile, and notched Charpy impact performance of the compatibilized rPP compounds are summarised in Figure 5. Figure 5a reports the MFI of the four formulations measured at 230 °C under a 2.16 kg load. All compounds fall within a narrow processing window of 14.8 to 16.8 g/10 min, confirming that the compatibilizer architecture preserves the melt flowability required for injection moulding. The iMA and biMA systems exhibit essentially identical MFI values of 14.8 and 14.9 g/10 min, whereas the pure aMA compound rises to 16.8 g/10 min and the Commercial benchmark sits at 15.6 g/10 min. The equivalence of iMA and biMA is mechanistically significant. Despite biMA containing 50 wt% of the low-molecular-weight aPP-*g*-MA (Mw ≈ 4208 g mol^{-1}), the bulk melt viscosity remains indistinguishable from the pure iMA formulation. A linear mixing expectation based on the iMA and aMA end-members would place biMA at approximately 15.8 g/10 min, yet the measured value closely tracks iMA. This deviation indicates that the amorphous aPP-*g*-MA component in the binary system preferentially localises at the matrix/defect interfaces, anchored by the co-crystallising iPP-*g*-MA fraction, which restricts its redistribution as a homogeneous bulk plasticizer. In the pure aMA system, the absence of an isotactic anchor releases the amorphous segments into the continuous phase, producing the highest MFI observed.

As presented in Figure 5b, the TS of all four formulations is confined to a narrow range of 20.5 to 21.5 MPa. The Commercial benchmark exhibits the highest TS at 21.5 MPa, directly correlating with the dense, load-bearing α-crystalline network provided by its pure isotactic backbone. The biMA formulation retains a tensile strength of 20.9 MPa, closely tracking the pure aMA (21.0 MPa) and marginally exceeding iMA (20.5 MPa). This narrow spread suggests that integrating the amorphous aPP-*g*-MA component does not severely compromise bulk rigidity, as the iPP-*g*-MA fraction within the binary blend preserves structural cohesion through co-crystallization with the rPP matrix. The baseline reinforcement from the talc filler is consistent across all four formulations and therefore does not account for the inter-group differences, which instead track the crystalline continuity of the compatibilizer/matrix interphase.

The definitive advantage of the binary compatibilization strategy emerges in the ductility and energy-dissipation metrics. Figure 5c,d reveal a pronounced non-monotonic enhancement in toughness. The biMA compound exhibits a marked improvement in elongation at break to 200%, representing a 203% increase over the iMA system (66%) and a 456% increase over the commercial benchmark (36%). A critical observation emerges from the pure aMA system, which fails to produce any ductility enhancement and in fact registers the lowest EB at 57%. Simultaneously, the impact strength of biMA reaches the highest level among all tested groups at 8.98 kJ m^{-2}. This value surpasses iMA (8.42 kJ m^{-2}), Commercial (8.53 kJ m^{-2}), and aMA (8.63 kJ m^{-2}). The compositional non-additivity of both EB and IS, in which biMA outperforms each individual end-member, supports a synergistic toughening mechanism rather than a simple linear superposition.

This synergistic toughening behaviour is consistent with the proposed compliant/crystalline interphase mechanism [16]. In single-component rigid systems such as iMA or the Commercial benchmark, the highly crystalline interphase lacks the necessary viscoelasticity to accommodate the severe stress concentrations surrounding the inherent micro-defects and heterogeneous inclusions within the post-consumer rPP. Consequently, these rigid interfaces readily initiate micro-cracks under load, leading to premature brittle failure and low EB. Conversely, the fully amorphous aMA system lacks sufficient crystalline anchoring, resulting in interface debonding before macroscopic stress can be effectively transferred. This interpretation is corroborated by the highest MFI observed in the aMA system, which indicates redistribution of the amorphous phase through the continuous

matrix rather than localisation at the defect interfaces, and is consistent with the lowest EB (57%) recorded among all four formulations.

The biMA formulation uniquely resolves this structural conflict. The amorphous aPP-*g*-MA component may provide a conformal, compliant buffer zone that helps wet and accommodate microscale defects, while the iPP-*g*-MA component provides crystalline anchoring with the bulk matrix. Under applied stress, this proposed defect-tolerant interphase blunts crack tips and facilitates extensive microfibrillar drawing and shear yielding. The macroscopic manifestation of this cooperative molecular architecture is the transition from brittle fracture to high ductility, supporting the efficacy of the binary compatibilizer in upcycling highly heterogeneous polymeric waste.

3.5. Microscopic Fracture Morphology and Toughening Mechanism

SEM of the tensile fracture surfaces provides morphological evidence consistent with the proposed defect-tolerant mechanism, rather than direct nanomechanical proof of a modulus gradient. As shown in Figure 6a, the low-magnification overview of the biMA formulation exhibits extensive macroscopic fibrillar elongation along the drawing direction. At a higher magnification of 2000× (Figure 6b), the surface reveals a hierarchically rough architecture characterised by dense micro-void arrays flanking elongated fibrillar bridges. This specific morphology is a classic indicator of a cavitation-assisted shear-yielding mechanism. Under triaxial stress, the amorphous aPP-*g*-MA domains localised at the defect interfaces may undergo preferential cavitation. This localised voiding relieves the triaxial constraint, blunts the stress concentration around the heterogeneous inclusions of the rPP matrix, and permits the surrounding matrix to undergo plastic deformation and energy dissipation prior to catastrophic failure [17,18]. This morphology was distinguished from simple interfacial debonding by the coexistence of embedded/encapsulated talc regions and matrix tearing in the biMA sample, whereas the aMA and commercial benchmark show more exposed talc, interfacial voids, and debonding features.

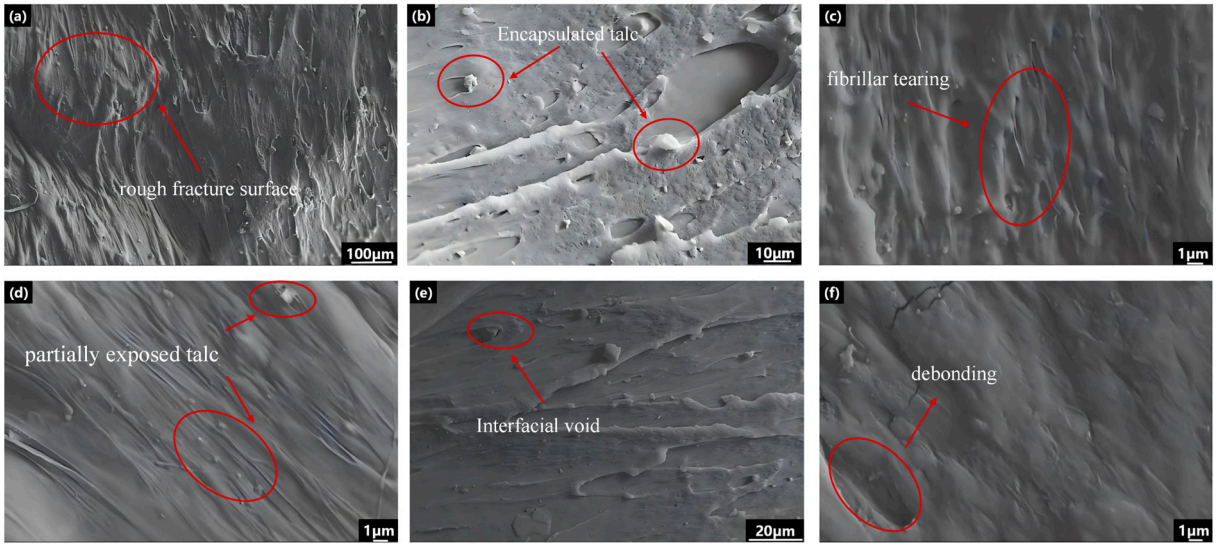


Figure 6. Scanning electron microscopy (SEM) images of tensile fracture surfaces: (**a**) biMA formulation at 300×; (**b**) biMA at 2000×; (**c**) biMA at 10,000×; (**d**) iMA at 10,000×; (**e**) aMA at 1000×; (**f**) Commercial benchmark at 10,000×. Red circles and arrows mark representative fracture features, including rough fracture surfaces, encapsulated talc, fibrillar tearing, interfacial voids, partially exposed talc, and debonding.

The critical role of the binary compatibilizer is further elucidated at the nanoscale. The biMA fracture surface (Figure 6c) presents a dense network of sub-micrometre fibrils

spanning the fracture plane. This microstructural homogeneity suggests that the aPP-*g*-MA and iPP-*g*-MA components function cooperatively: the soft aPP segments accommodate micro-defect-associated stress concentrations, while the crystalline iPP segments establish tie-molecule networks with the bulk rPP, stabilising the fibrils against premature rupture during drawing [19].

In stark contrast, the aMA formulation (Figure 6e) exhibits a markedly distinct failure mode. The surface is characterised by broad lamellar tearing, massive macroscopic voids, and a severe lack of fine fibrillar bridges. This topology validates that relying solely on a highly mobile amorphous compatibilizer is insufficient: without the crystalline anchoring capability provided by the isotactic backbone, the soft aPP-*g*-MA layer simply debonds from the rPP matrix under stress, leading to inter-spherulitic delamination and low macroscopic toughness.

The SEM comparison was used to identify representative fracture features and to correlate the dominant interfacial failure mode with the mechanical trends. The iMA (Figure 6d) and Commercial (Figure 6f) formulations present fundamentally similar morphologies featuring localised fibrillar structures interspersed with rigid, undeformed domains. The absence of the compliant aPP phase renders these crystalline interphases too rigid to accommodate the diverse defect structures inherent in post-consumer rPP. Consequently, these interfaces fail to effectively dissipate energy around critical defect sites, resulting in the localised crack propagation and lower elongation at break observed in macroscopic mechanical testing. The structural evolution from localised tearing (aMA) and restricted drawing (iMA) to widespread, uniform fibrillation (biMA) supports the proposed synergistic efficacy of the compliant/crystalline interphase.

4. Conclusions

A defect-tolerant binary compatibilizer system comprising iPP-*g*-MA and aPP-*g*-MA was developed to address the structural heterogeneity of post-consumer recycled PP derived from disposable meal containers. The revised evidence supports a proposed compliant/crystalline interfacial architecture in which the amorphous aPP-*g*-MA component accommodates localised defect-associated stress concentrations while the iPP-*g*-MA component provides crystalline anchoring to the bulk matrix. This interfacial architecture effectively translates macroscopic stress into extensive microfibrillar drawing and shear yielding. The optimised equal-weight biMA formulation yields an elongation at break of 200% and an impact strength of 8.98 kJ m^{-2}, exceeding the commercial benchmark values of 36% and 8.53 kJ m^{-2}. Tensile strength is preserved at 20.9 MPa. TGA further shows no premature degradation within the PP melt-processing window, supporting thermal suitability for melt reprocessing. This work establishes a scalable and physically grounded pathway for the mechanical upcycling of highly degraded polyolefin waste streams. Nevertheless, long-term thermo-oxidative aging, outdoor weathering resistance, continuous pilot-scale processing, and applicability to other mixed polyolefin waste streams require further evaluation. These results imply that compatibilizer design for heterogeneous rPP should target defect-rich interfaces by combining stress-transfer anchoring with local interfacial compliance, rather than relying only on bulk crystallinity or polarity.

Author Contributions: R.L.: Conceptualization, Software, Data Curation, Writing—Original Draft Preparation. H.C.: Validation, Formal Analysis, Investigation. Z.T.: Validation, Resources. L.T.: Conceptualization, Methodology, Validation, Writing—Review and Editing, Visualization, Supervision, Project Administration, Funding Acquisition. All authors have read and agreed to the published version of the manuscript.

Funding: This research was supported by the China Postdoctoral Science Foundation (2025M770125), the Natural Science Foundation of Jiangxi Province (20252BAC240243), the Over-seas Talent Introduction Program of Jiangxi Province (20232BCJ25061), the High-level Talent Re-search Start-up Fund of Jiangxi University of Science and Technology (205200100632), the Key Scientific and Technological Research Project of Jiangxi Provincial Department of Education (GJJ2200821), the Key Laboratory of Functional Crystal Materials Chemistry of Jiangxi Province (2024SSY05161), and the Key Laboratory of Functional Molecular Materials Chemistry of Jiangxi Province (20212BCD42018).

Data Availability Statement: The data presented in this study is available on request from the corresponding author. The data is not publicly available due to ongoing related research.

Acknowledgments: The authors gratefully acknowledge the analysis and testing center of Jiangxi University of Science and Technology for technical support in materials characterization.

Conflicts of Interest: Authors Haidi Cai and Zhonghua Tang were employed by Jiangxi Yameda Technology Co., Ltd. The remaining authors declare that the research was conducted in the absence of any commercial or financial relationships that could be construed as a potential conflict of interest.

References

1. Geyer, R.; Jambeck, J.R.; Law, K.L. Production, Use, and Fate of All Plastics Ever Made. *Sci. Adv.* **2017**, *3*, e1700782. [CrossRef] [PubMed]
2. Borrelle, S.B.; Ringma, J.; Law, K.L.; Monnahan, C.C.; Lebreton, L.; McGivern, A.; Murphy, E.; Jambeck, J.; Leonard, G.H.; Hilleary, M.A.; et al. Predicted Growth in Plastic Waste Exceeds Efforts to Mitigate Plastic Pollution. *Science* **2020**, *369*, 1515–1518. [CrossRef] [PubMed]
3. Ragaert, K.; Delva, L.; Van Geem, K. Mechanical and Chemical Recycling of Solid Plastic Waste. *Waste Manag.* **2017**, *69*, 24–58. [CrossRef] [PubMed]
4. Prior, L.; Oliveira, M.S.A.; Zhiltsova, T. Assessment of the Impact of Superficial Contamination and Thermo-Oxidative Degradation on the Properties of Post-Consumer Recycled Polypropylene. *Materials* **2023**, *16*, 1198. [CrossRef] [PubMed]
5. Veroneze, I.B.; Onoue, L.A.; Cruz, S.A. Thermal Stability and Crystallization Behavior of Contaminated Recycled Polypropylene for Food Contact. *J. Polym. Environ.* **2022**, *30*, 3474–3482. [CrossRef] [PubMed]
6. Tumu, K.; Vorst, K.; Curtzwiler, G. Comparison of Recycled Polypropylene Sourced from Food and Nonfood Applications for Direct Food Contact Use. *Packag. Technol. Sci.* **2026**, *39*, e70059. [CrossRef]
7. Schyns, Z.O.G.; Shaver, M.P. Mechanical Recycling of Packaging Plastics: A Review. *Macromol. Rapid Commun.* **2021**, *42*, 2000415. [CrossRef] [PubMed]
8. Tariq, A.; Ahmad, N.M.; Abbas, M.A.; Shakir, M.F.; Khaliq, Z.; Rafiq, S.; Ali, Z.; Elaissari, A. Reactive Extrusion of Maleic-Anhydride-Grafted Polypropylene by Torque Rheometer and Its Application as Compatibilizer. *Polymers* **2021**, *13*, 495. [CrossRef] [PubMed]
9. Andrés Riveros Muñoz, P.; Cornelius Bonse, B.; Vicente Canevarolo, S.; Helena Prado Bettini, S. Kinetics in High-Temperature Free-Radical Reactive Processing: Grafting Maleic Anhydride onto Polypropylene in the Presence of Nanoclay-Supported Peroxide. *Chem. Eng. Sci.* **2024**, *298*, 120319. [CrossRef]
10. Bettini, S.H.P.; Agnelli, J.A.M. Grafting of Maleic Anhydride onto Polypropylene by Reactive Extrusion. *J. Appl. Polym. Sci.* **2002**, *85*, 2706–2717. [CrossRef]
11. Collins Rice, C.G.; Buffet, J.-C.; Turner, Z.R.; O'Hare, D. Efficient Synthesis of Thermoplastic Elastomeric Amorphous Ultra-High Molecular Weight Atactic Polypropylene (UHMWaPP). *Polym. Chem.* **2022**, *13*, 5597–5603. [CrossRef]
12. Cui, Y.; Shi, H.; Zhang, Y.; Cui, L.; Zhao, W.; Liu, W. Experimental Investigation on Air Gasification of Polypropylene Particles in a Microwave Fluidized Bed Reactor. *Ind. Eng. Chem. Res.* **2023**, *62*, 17306–17313. [CrossRef]
13. Qiu, Z.; Li, X.; Wu, H.; Zhao, S. A New Method for Preparing Anhydride Grafted Polypropylene with High Grafting Ratio by Combining Microwave Reaction and Reactive Extrusion. *J. Polym. Res.* **2023**, *30*, 319. [CrossRef]
14. Świetlicki, M.; Chocyk, D.; Klepka, T.; Prószyński, A.; Kwaśniewska, A.; Borc, J.; Gładyszewski, G. The Structure and Mechanical Properties of the Surface Layer of Polypropylene Polymers with Talc Additions. *Materials* **2020**, *13*, 698. [CrossRef] [PubMed]
15. Zhan, K.; Elder, T.; Peng, Y. Enhancing Polypropylene/Polyethylene Blend Performance Through Compatibilization for a Sustainable Future: A Mini Review Focusing on Establishing Bio-Derived Filler Based Hybrid Compatibilizer System. *Macromol. Rapid Commun.* **2025**, *46*, 2400724. [CrossRef] [PubMed]
16. Wei, J.; Abdurexit, A.; Jamal, R.; Abdiryim, T.; You, J.; Li, Z.; Shang, J.; Cheng, Q. Carbon Fiber Reinforced Recycled Polypropylene/Polyolefin Elastomer Composites with High Mechanical Properties. *Polymers* **2024**, *16*, 972. [CrossRef] [PubMed]
17. Argon, A.S.; Cohen, R.E. Toughenability of Polymers. *Polymer* **2003**, *44*, 6013–6032. [CrossRef]

18. Pawlak, A.; Galeski, A. Cavitation during Tensile Deformation of Polypropylene. *Macromolecules* **2008**, *41*, 2839–2851. [CrossRef]
19. Nitta, K.-H.; Takayanagi, M. Role of Tie Molecules in the Yielding Deformation of Isotactic Polypropylene. *J. Polym. Sci. B Polym. Phys.* **1999**, *37*, 357–368. [CrossRef]

Disclaimer/Publisher's Note: The statements, opinions and data contained in all publications are solely those of the individual author(s) and contributor(s) and not of MDPI and/or the editor(s). MDPI and/or the editor(s) disclaim responsibility for any injury to people or property resulting from any ideas, methods, instructions or products referred to in the content.